Faraday Discussions

Modulating Donor-Acceptor Transition Energies in Phosphorus-Boron co-Doped Silicon Nanocrystals via X- and L-Type Ligands

Journal:	*Faraday Discussions*
Manuscript ID	FD-ART-10-2019-000106.R1
Article Type:	Paper
Date Submitted by the Author:	06-Dec-2019
Complete List of Authors:	Pach, Gregory; National Renewable Energy Laboratory, Chemistry and Nanoscience Carroll, Gerard; National Renewable Energy Laboratory, Chemistry and Nanoscience Zhang, Hanyu; national renewable energy laboratory, Nanoscience and Chemistry Neale, Nathan; National Renewable Energy Laboratory,

ARTICLE

Modulating Donor-Acceptor Transition Energies in Phosphorus-Boron co-Doped Silicon Nanocrystals via X- and L-Type Ligands

Received 00th January 20xx,
Accepted 00th January 20xx

DOI: 10.1039/x0xx00000x

Gregory F. Pach,[a] Gerard M. Carroll,[a] Hanyu Zhang,[a] Nathan R. Neale*[a]

In this work, we explore the effect of ligand binding groups on the visible and NIR photoluminescent properties within phophorus-boron co-doped silicon nanocrystals (PB:Si NCs) by exploiting both the X-type (covalent) and L-type (Lewis donor molecule) bonding interactions. We find that the cooperative nature of both X- and L-type bonding from alkoxide/alcohol, alkylamide/alkylamine, and alkylthiolate/alkylthiol on PB:Si NCs results in photoluminescence (PL) energy blue shifts from the as-synthesized, hydride-terminated NCs (PB:Si–H) in excess of 0.4 eV, depending on the surface termination. These PL blue shifts appear greatest in the most strongly confined samples with diameters <4 nm where the surface-to-volume ratio is high and, therefore, the ligand effects are most pronounced. A correlation between the donor group strength (either X-type or L-type) and the degree of D–A state modulation is found, and the proportion of the PL blue shift from the X- and L-type interactions is quantified. Raman spectroscopy is used to provide additional evidence of the strength of the L-type donor groups. Additionally, we probe how the nature of the ligand chemistry affects the radiative lifetime and PL efficiency and find that the ligands do not significantly change the D–A emission dynamics, and all samples retain the long 50–130 μs lifetimes characteristic of these transitions. Finally, we describe three mechanisms that operate to effect the D–A recombination energies: (1) X-type ligands that modulate the PB:Si–X NC wavefunction; (2) L-type ligands that perturb the donor and acceptor states via a molecular orbital theory picture; and (3) X- and L-type ligands that cause a dielectric increase around the PB:Si NC core, which provides Coulomb screening and modulates the donor and acceptor states even further.

Introduction

Quantum-confined semiconducting nanocrystals (NCs) have drawn considerable interest for light emitting applications due to their size-tunable optical properties and high quantum yields.[1, 2] The ubiquity of Si in the electronics industry as well as its low toxicity warrants Si NCs as particularly interesting candidates for near-infrared (NIR) emission applications in which the majority of materials contain heavy metals and/or use toxic synthetic precursors.[3, 4] However, two limitations of Si are its indirect, rather than direct, band gap that is 1.1 eV in bulk. The indirect optical gap results in poor visible light absorption, though it is possible to modulate the absorption coefficient through quantum confinement[5] and for some applications the large Stokes shift afforded by this property is actually desirable, for example in luminescent solar concentrators.[6] In addition, though quantum confinement pushes the band gap emission to the visible region,[7] several studies have shown that the incorporation of impurity dopants into semiconducting NCs can be used to further tune the optical properties of NC ensembles.[8-10] For example, for two decades it has been known that doping Si NCs with substitutional phosphorus or boron dopant atoms results in sub-band gap emission due to interaction of the exciton with the dopant state.[11, 12]

To this end, nonthermal plasma synthesis of semiconductor NCs provides a particular synthetic advantage for dopant incorporation by circumventing the “self-purification effect” in which impurity atoms are expelled from the NC core to the surface.[13, 14] This is because nonthermal plasma synthesis is a kinetic growth process occurring out of equilibrium that can irreversibly trap dopants within the core. This process has been widely used to dope Si NCs with phosphorus and boron impurities.[15-20] Expanding upon these single dopant systems, a recent publication from our group also has demonstrated the ability to use nonthermal plasma synthesis to simultaneously incorporate both boron and phosphorus dopants into co-doped Si NCs (PB:Si).[21] Delerue described the emission properties of these PB:Si NCs as purely governed by donor-acceptor (D–A) transitions attributed to charge-compensating phosphorus-boron (P-B) pairs.[22] Consequently, our results showed that the peak emission energy of these plasma-synthesized

[a] *Chemistry and Nanoscience Center, National Renewable Energy Laboratory, 15013 Denver West Parkway, Golden, Colorado 80401, United States.*
* Corresponding author Email: nathan.neale@nrel.gov
Electronic Supplementary Information (ESI) available: [details of any supplementary information available should be included here]. See DOI: 10.1039/x0xx00000x

PB:Si NCs is consistently red shifted several hundred meV from that of intrinsic Si NCs of the same diameter, below the bulk 1.1 eV band gap at lightly quantum-confined NCs (diameters >4 nm). The results from plasma-synthesized PB:Si NCs is in line with many prior studies on co-doped PB:Si NCs fabricated using thermal precipitation from phosphoborosilicate glass.[23-28]

More generally, the large surface-to-volume ratio of nanostructures results in the surface playing a critical role in dictating the NC optoelectronic properties, and the ability to control these properties via controlled surface chemistry is now widely established.[29-31] In Si NCs, there are three known methods of controlling the optoelectronic properties: (1) quantum confinement to tune the band edge emission as originally demonstrated by Brus et al. in 1993;[32] (2) supra-band gap oxide and/or nitrogen-related defect state emission described by the seminal work of Tilley, Kauzlarich, Veinot and coworkers in 2013;[33] and (3) intentional surface chemistry manipulation. The latter method can be broken up into several sub-categories including (i) Lewis acid-base interactions via donor molecule coordination to either polarized Si surface atoms or surface heteroatoms,[20, 34] (ii) coupling of π-conjugated ligand molecular orbitals to the Si NC wavefunction,[35, 36] and (iii) covalent surface group modification including halogens *Si–X (where *Si denotes a surface Si atom; X = Cl, Br, I)[37] or other main group ligands *Si–ER group (where E = CH_2, NH, O, S; R = alkyl).[38, 39] Theoretical frameworks exist for the surface interactions on Si NCs based on changing the dielectric matrix described by Luo and Zunger[40] or altering the bonding structure at the Si NC surface introduced by Galli and Kimerling.[41]

For covalent ligand attachment to Si NCs, surface functionalization is conventionally performed via a radical reaction involving the removal of a surface hydrogen atom (H•) or silyl group (•SiH_3) and substitution with a covalent ligand bond.[42, 43] In our recent studies, we demonstrated the use of a variety of surface terminations on Si NCs including alkyls (from reaction with 1-dodecene), alkoxides (1-dodecanol), secondary amides (1-dodecylamine), and thiolates (1-dodecanethiol).[38, 39] We proposed that the ligand head group (the only atoms that change via this chemistry) interact with the Si NC electronic wave function and, depending on the ligand, modulate the peak photoluminescence (PL) emission energy by up to ~150 meV for small NC sizes (~3 nm). In addition to covalent functionalization, we have pioneered Lewis acid-base interactions that either create or perturb the localized surface plasmonic resonance (LSPR) in Si NCs.[20, 34] To date there are no studies describing whether these Lewis acid-base interactions also can be employed to control the emission properties in Si NCs since previously all such interactions are on doped NCs that do not exhibit band edge luminescence.

In this report, we explore the effect of ligand binding groups on the visible and NIR photoluminescent properties within PB:Si NCs by exploiting both the X-type (covalent) and L-type (Lewis donor molecule) bonding interactions classically described by Green.[44] We explore both the individual and cooperative nature of both X- and L-type bonding, which results in PL energy shifts from the as-synthesized, hydride-terminated NCs (PB:Si–H) in excess of 0.4 eV, depending on the surface termination. We probe the emission energies as a function of size and find correlation between the donor group strength (either X-type or L-type) and the degree of D–A state modulation, and additionally quantify the proportion of the PL blue shift from the X- and L-type interactions. We also probe how the nature of the ligand chemistry affects the radiative lifetime and PL efficiency as well as vibrational states within the PB:NCs via Raman spectroscopy. Finally, we describe three mechanisms that operate to effect the D–A recombination energies based on these experiments.

Results

All PB:Si NCs in this study were synthesized using a capacitively-coupled 13.56 MHz nonthermal plasma with process gases SiH_4, B_2H_6, and PH_3 and additional carrier gases Ar and H_2 (see Table S1 for process conditions of all PB:Si NCs used in this study). As-synthesized co-doped PB:Si–H NCs are terminated with surface hydride groups that are readily distinguishable via FTIR (Figure S1). Surface silicon hydride groups *SiH (ν = 2087 cm^{-1}), *SiH_2 (ν = 2108 cm^{-1}), and *SiH_3 (ν = 2138 cm^{-1}) are present, where the asterisk (*) denotes a surface atom, as well as surface dopants such as *PH_x (ν = 2276 cm^{-1}); larger size NCs additionally exhibit *BH_x (ν ~ 2500 cm^{-1}).[21] Notably, a LSPR is absent in the FTIR spectra of these hydride-terminated PB:Si (PB:Si–H) NCs, which can be attributed to near-perfect charge compensation between charges introduced from donor and acceptor impurities.[21] The NC size is determined via XRD and the Scherrer broadening of the (111) diffraction peak (Figure S2) correlates well with our experimentally determined PL sizing curve.[43] Additional evidence of dopant atom incorporation also can be seen through a continual shift of the (111) diffraction peak to higher angles with increasing NC size, representing a smaller lattice constant consistent with a greater number of substitutional boron sites.[20]

The nanoparticle surface can be modified post-synthesis to render PB:Si NCs colloidally dispersible. Covalent functionalization of PB:Si NCs follows our previously reported procedure for intrinsic Si NCs[38, 43] by heating hydride-terminated PB:Si–H NCs in neat reactant (1-dodecene, 1-dodecanethiol, 1-dodecylamine, or 1-dodecanol) at 140–150 °C for ~4 h with the addition of 1,1'-azobis(cyclohexanecarbonitrile) radical initiator (see Experimental for full details). Hydride (as-synthesized) and alkyl (from reaction with 1-dodecene) groups bind solely via an X-type interaction at the surface of PB:Si–X NCs (Figure 1), where the X-type

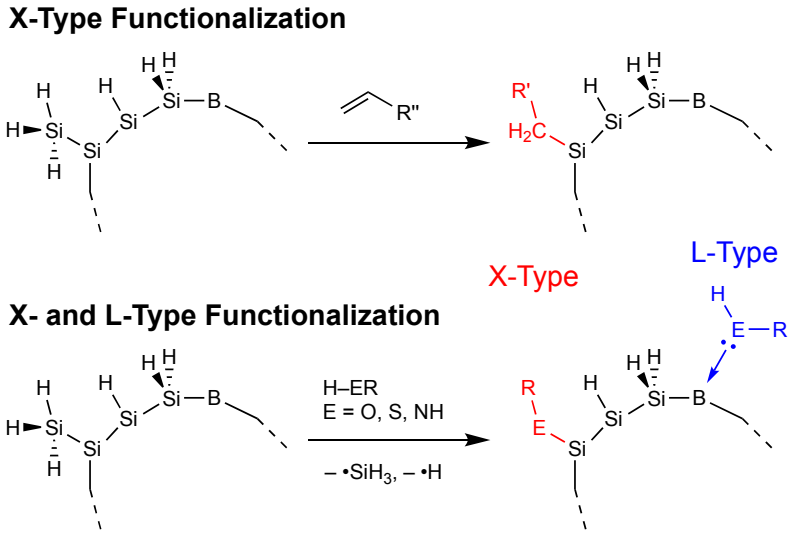

Fig. 1 Schematic illustration of the X- and L-Type functionalization mechanisms for PB:Si NCs. X-type functionalization involves the formation of a covalent bond with a surface *Si atom, whereas L-type functionalization is Lewis donor molecule coordination to a surface Lewis acidic *B atom.

formalism refers to a covalent bond between a ligand and metal (in this case silicon).[44] In addition to conventional X-type ligation, highly Lewis-acidic boron sites reside at the NC surface in a three-coordinate arrangement allowing acid-base interactions.[20, 45-47] It has been shown that boron atoms are primarily incorporated on the NC surface as opposed to the core due to reduced solubility of boron within the NC core caused by the mismatch in atomic radii between B and Si.[45] As evident by spontaneous solubility of as-synthesized boron-doped silicon (B:Si) NCs in strongly polar solvents such as methanol, N-methylpyrrolidone (NMP), and dimethylsulfoxide (DMSO), the electron pair from a filled O 2p orbital in the donor molecule bonds via dative interaction with the empty 2p orbital of the surface boron atoms.[21] This type of bonding interaction is classified by Green as L-type, where both electrons are provided by the ligand interactions.[44] Three of the surface ligands studied in this report (1-dodecanethiol, 1-dodecylamine, and 1-dodecanol) have Lewis basic head groups that bond via such an L-type interaction with surface *B in addition to X-type bonding. We notate these species L→PB:Si–X throughout this work.

Figure 2 summarizes experimental PL results and details how the emission energy can be modified by changing the surface termination of PB:Si NCs (see Figure S3 for all emission profiles). The expected peak emission energy for alkyl-terminated intrinsic Si NCs as a function of the NC diameter (D_{NC}) can be approximated using an empirically developed $D_{NC}^{-1.69}$ dependence (Figure 2b, black dashed trace).[43] The peak emission energy of the PB:Si–H NCs (Figure 2b, gray points) is consistently ~400 meV red-shifted from that of the intrinsic Si NC trend across all sizes within the confinement regime, owing to lower energy D–A transitions, and follows a slightly different power dependence of $D_{NC}^{-2.09}$.[21] We find PB:Si–H NCs synthesized in this study to still follow this dependence showing the reproducibility of the plasma growth process (Figure S4). Subsequent functionalization and solubilization of PB:Si–X and L→PB:Si–X NCs blue-shifts the emission relative to the as-synthesized PB:Si–H NCs for all functional groups studied. The greatest shift is induced by cooperative alcohol/alkoxide terminations that display changes in the emission energy of over 400 meV. Unlike intrinsic Si NCs with alkoxide surface chemistry that exhibit a size-dependent band edge emission (where stronger *Si–OR effects are observed for the smaller, more quantum-confined NCs[38]), the change in the D–A emission energy for each L→PB:Si–X functionalized NC across the entire size range studied here (2.7–5.1 nm) is only ~50 meV (Figure S5). The fact that the smallest shift results from X-type-only interactions through alkyl (*Si–CH_2R) bonding suggests that Lewis acid-base interactions at the NC surface also influence the PB:Si NC electronic structure of the donor and acceptor states.

We next attempt to quantify the individual effects of the covalently bound X-type and coordinated L-type ligands. Similar to Fujii's original report of dispersion of PB:Si NCs in methanol,[26] we find that PB:Si–H NCs directly disperse in a solution of toluene and 1-dodecanol or 1-dodecylamine at room temperature (Figure S6). In contrast, similar experiments with 1-dodecanethiol in toluene do not induce spontaneous suspension. We suspect that these solubility differences result from two effects. First, the weaker nature of the Lewis acid-base complex with thiols (i.e., RHS→*B) relative to that with alcohols and alkylamines does not provide sufficient energy for solvation.[47] Second, the PL spectra from the functionalized L→PB:Si–X NCs produced via either the spontaneous solubilization process or the radical-initiated thermal functionalization route align nearly exactly (Figure S7a). We therefore hypothesize that the dispersion process in protic reagents such as alcohols and amines does *not* interact solely via Lewis

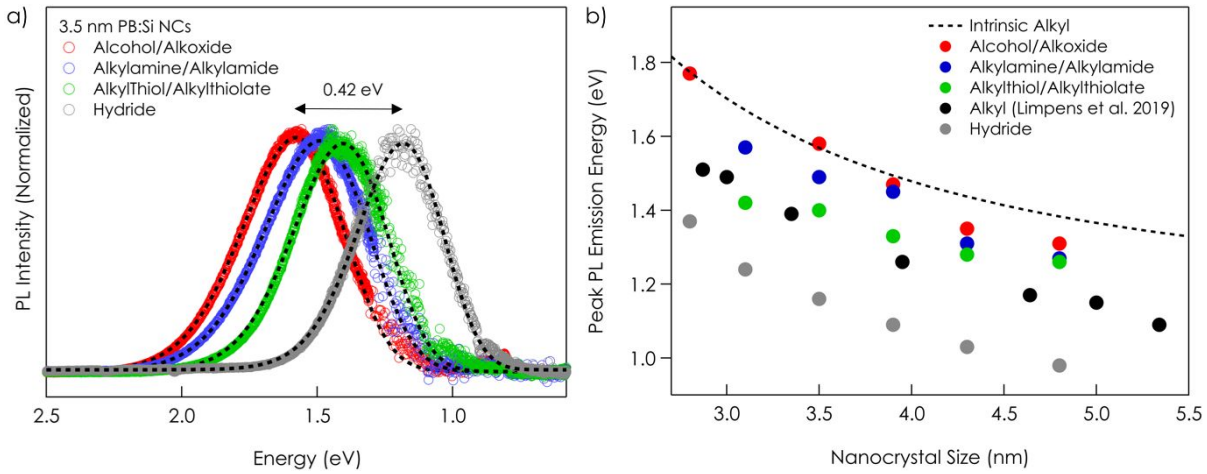

Fig. 2 (a) Representative shifts in the peak PL emission energy from 3.5 nm RHO→PB:Si–OR (red), RH_2N→PB:Si–NHR (blue), and RHS→PB:Si–SR (green) NCs. All traces are fit with a lognormal (black dashed traces) (b) Summary of the peak PL energies for a variety of PB:Si NC sizes and surface chemistries. Peak PL energies from alkyl-functionalized PB:Si–CH_2R NCs are included from our previous study.[21]

acid-base chemistry, and that reaction to generate X-type ligands also occurs at ambient conditions. Our previous study of the mechanism of radical-initiated surface reactions on nonthermal plasma-synthesized intrinsic Si NCs showed that abstraction of surface silyl groups, *SiH_3, can occur spontaneously at room temperature[43] that can explain our observation here. In addition, we find that FTIR spectra from B:Si NCs solvated in DMSO (termed "DMSO–B:Si" in our prior work[20]) exhibit a strong absorption at ~2240 cm^{-1} characteristic of the so-called 'back-bonded' Si–H stretch, where a high frequency ~2240 cm^{-1} Si–H vibration results from the *Si atom also being bound to a highly electron-withdrawing oxygen atom, (O)*SiH_x. Since coordination of DMSO via an L-type interaction as $(CH_3)_2$(O)S=O→PB:Si cannot be the source of this IR absorption feature—there is no strongly affected *SiH_x vibration via this L-type interaction since it bonds to a surface boron atom—we posit that this high energy Si–H stretch results from hydro- and/or silylsilylation across the sulfoxide S=O bond in DMSO to give an X-type ligand $(CH_3)_2$(O)(Y)S–O–*SiH_x (Y = H for hydrosilylation and SiH_3 for silylsilylation) in addition to a L-type interaction. See Figure S8 for full description of the reaction with DMSO.

Additional confirmation that the shifts in PL energy in Figure 2 must be attributed to both X-type and L-type interactions is derived from an experiment in which 3.5 nm PB:Si NCs are successively functionalized with covalent and then dative ligands. PB:Si NCs are first functionalized with covalent alkyl groups using the radical-initiated thermal method. After collecting the PL spectrum of the resulting PB:Si–CH_2R NCs, a small amount of 1-dodecanol is added to the toluene solution in the cuvette. As shown in Fig. S7b, the resulting PL spectrum of the alcohol/alkyl RHO→PB:Si–CH_2R NCs blue shifts by ~50 meV from the alkyl-only PB:Si–CH_2R NCs. These data provide clear evidence that both types of surface chemistry interactions affect the energy of the D–A recombination in PB:Si NCs. In addition, this experiment allows us to quantify the shift derived from alcohol L-type coordination to surface *B atoms at ~50 meV. Since the PL energy of 3.5 nm diameter alcohol/alkoxide RHO→PB:Si–CH_2R are blue-shifted by ~200 meV relative to alkyl-only PB:Si–CH_2R (Fig. 2), this additionally means that X-type ligation with alkoxide results in ~150 meV PL blue shift relative to alkyl. Thus, the effect of X-type ligation on D–A transition energies in PB:Si NCs appears to be similar to that for our prior report on this ligand head group effect on the band edge emission energies in intrinsic Si NCs for small NC sizes (<4 nm). [38]

To probe possible changes to the radiative mechanism, we characterize the radiative lifetimes of L→PB:Si–X Si NCs using time-resolved photoluminescence (TRPL) spectroscopy. Figure 3a shows representative TRPL traces for 3.5 nm L→PB:Si–X NCs. The effective lifetime is retrieved by fitting a single exponential to the dominant, long-lived component of the decay. Figure 3b summarizes the lifetimes of several different sized functionalized samples with alkyl, alkylamine/alkylamide, alcohol/alkoxide, and alkylthiol/alkylthiolate surface terminations (see Figure S9 for all TRPL data and fits). The lifetimes of all L→PB:Si–X NCs, irrespective of the ligands, are found to be slightly faster than what is found of alkyl-terminated, intrinsic Si NCs of the same size (Figure 3b, black dashed trace) consistent with Fujii and our prior reports.[21, 26, 48] While D–A recombination is generally expected to be a slow, tunneling process, the slightly faster effective lifetime is most likely due to a convolution of different radiative decay pathways.[49] From the shape of the TRPL decay, it is evident that multiple decay pathways indeed exist. These traces can be fit using a multi-exponential fit (Figure S10) that can quantify the various distinct decay pathways. Another of our studies has revealed that functionalizing Si NCs with alkylthiolate ligands can induce mid-gap trap states that contribute to Shockley-Read-Hall (SRH) -

type recombination.[39] This is reflected in the large amplitude decay within the first 20 μs in the RHS→PB:Si–SR TRPL trace as seen in Figure 3a and all RHS→PB:Si–SR traces in Figure S9. In agreement with an additional alkylthiol/alkylthiolate-derived recombination pathway, the PLQY of L→PB:Si–X samples exhibit a vast disparity in the radiative recombination efficiency of alcohol/alkoxide- and alkylamine/alkylamide-terminated PB:Si NC ensembles (both 12–13%) compared with alkylthiol/alkylthiolate terminations (2%) (Figure S11).

To further help elucidate the different surface environments in L→PB:Si–X and PB:Si–X NCs, we use Raman spectroscopy to examine the nature of the local boron mode upon different surface functionalizations. Collecting the Raman spectrum for RH_2N→PB:Si–NHR NCs proved difficult due to excess ligand that forms a solid at room temperature and induced overwhelming scattering of the Raman signal. RH_2N→PB:Si–NHR NCs are therefore not included in this analysis. As shown in Figure 4, two Raman modes of the as-synthesized PB:Si–H NCs at 498 cm^{-1} and ~600 cm^{-1} are attributed to the silicon LO phonon mode (broadened and made asymmetric by Fano interferrence[50]) and boron-related local vibrational modes, respectively. The LO phonon mode of silicon shifts by 18 cm^{-1} to 516 cm^{-1} upon functionalization. This may be related to reconstruction of surface hydrides upon thermal treatment during ligation which has been hypothesized to also enhance the PLQY.[51] Assignment of the B-related local vibrational

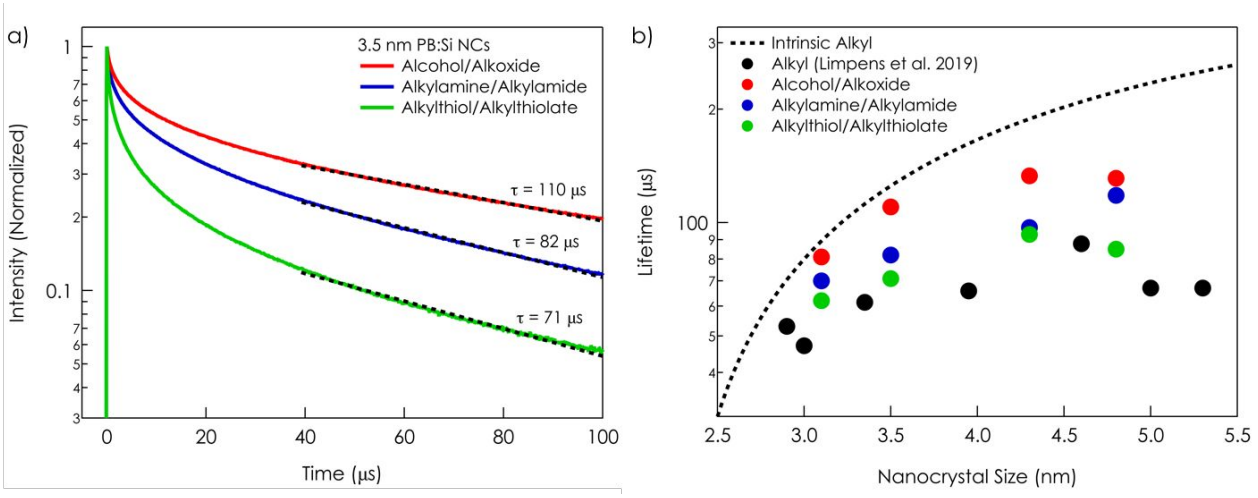

Fig. 3 (a) Representative TRPL traces from 3.5 nm RHO→PB:Si–OR (red), RH_2N→PB:Si–NHR (blue), and RHS→PB:Si–SR (green) NCs. Effective lifetimes are calculated by fitting the tail of the decay to a single exponential (black dashed traces). (b) Summary of all TRPL lifetimes acquired for multiple NC sizes and surface terminations (see Figure S9 for all TRPL traces). Lifetimes from alkyl-terminated PB:Si–CH_2R NCs are included from our previous study.[21]

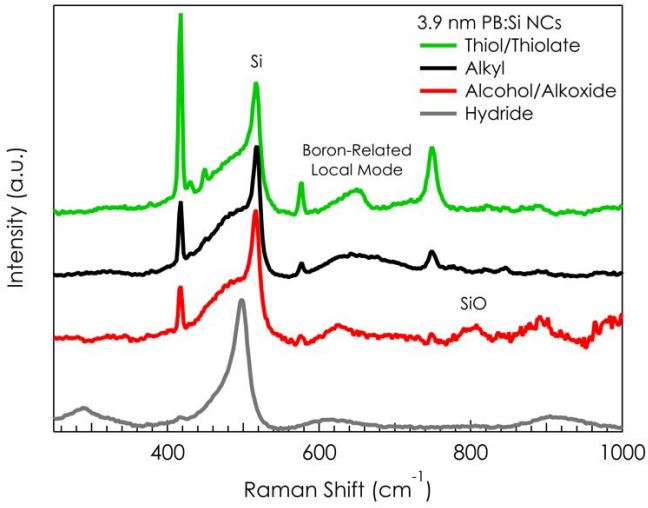

Fig. 4 Raman spectra of 3.9 nm RHS→PB:Si–SR (green), PB:Si–CH_2R (black), RHO→PB:Si–OR (red), as well as PB:Si–H NCs (gray) NCs. Strong, sharp peaks at 415–450, 577, and 750 cm^{-1} can all be attributed to the sapphire substrate (See Figure S12 for blank sapphire Raman spectrum).

mode is derived from previous Raman studies on PB:Si NC systems.[46, 52] Somogyi et al. modeled the vibrational density of states (VDOS) within PB:Si NCs and showed a large density of boron states extending from 600 to 800 cm^{-1} that could be attributed to disperse boron environments within PB:Si NCs (i.e., surface or core states, proximity to phosphorus atoms, coordination environment, etc.).[52] Generally, the high-energy tail of this broad peak has been attributed boron at the surface, and thus can provide a picture of the boron environment at the PB:Si surface. Upon surface functionalization, the boron mode is affected uniquely by the identity of the ligand binding group. For the RHO→PB:Si–OR and RHS→PB:Si–SR NCs, the boron mode shifts and narrows; a signature of different local environments. In contrast, the alkyl-terminated PB:Si–CH_2R NCs remains as a broad peak, indicating that the Lewis acid-base interaction with surface boron atoms *B is responsible for the narrowing. The direction of the energy shift is also ligand dependent. Whereas the RHO→PB:Si–OR results in a shift to lower energies relative to the H–PB:Si, the RHS→PB:Si–SR shows just the opposite. This shift is likely reporting on the strength of the acid-base interaction at the surface of the L→PB:Si–X NCs. In sum, the shift and sharpening of the B-related local Raman mode observed within RHO→PB:Si–OR and RHS→PB:Si–SR NCs is clearly attributed to L-type interactions at the NC surface.

Discussion

The mechanism accounting for the blue-shifted emission energy upon functionalization of PB:Si NCs is multi-faceted. To fully explain this picture, the different radiative mechanisms between PB:Si NCs and intrinsic Si NCs must first be understood. Delerue recently employed atomistic tight-binding calculations to model the specific energy levels created by phosphorus and boron impurities within PB:Si NCs.[22] The results show that close, but not nearest-neighbor, P-B pairs account for the D–A transitions observed experimentally. Furthermore, the extent of the PL red shift is largely dependent on the number of P-B pairs within the NC where even a single P-B pair shows a large impact on the radiative energy. It's important to note that phosphorus and boron impurities are only optically active when in a silicon substitutional site (i.e., in a four-coordinate arrangement). Therefore, trivalent boron atoms on the NC surface do not contribute to the effective number of P-B pairs. Based on Delerue's calculations, we estimate between 5 and 10 optically active P-B pairs within our PB:Si–H NCs that accounts for the 400 meV shift in emission energy from that of intrinsic Si NCs. The fact that such large shifts are seen for a relatively few number of optically active dopants is a result of the dielectric confinement effect in which partially unscreened Coulomb interactions create much deeper donor and acceptor levels than what is typically observed for impurity states in bulk Si.[22] It follows that different dielectric media surrounding the PB:Si NC will impact the level of confinement (greater Coulomb interactions for a greater mismatch in the dielectric constant) and subsequently the D–A energy levels. The changing emission energies from PB:Si–H to L→PB:Si–X and PB:Si–CH_2R NCs can therefore partially be explained by the changing dielectric medium between NC ensembles measured as free-standing powders (PB:Si–H) and in colloidal solutions (L→PB:Si–X and PB:Si–CH_2R). The more closely matched dielectric constants of the Si core with its ligands and solvent shell (compared with argon glove box atmosphere and hydride surface atoms for PB:Si–H) should increase the Coulomb interaction (decrease the Coulomb screening) and create shallower D–A energy levels, thereby blue-shifting the emission from PB:Si–H NCs.

In addition to dielectric effects, our prior study has shown that there is interaction of covalent X-type ligands and the Si NC wavefunction[38] that undoubtedly is responsible for some of the PL blue shift upon functionalization. This X-type ligand effect on the degree of exciton localization occurs not just for Si NCs but also metal chalcogenide quantum dots, where exchanging hard carboxylate or amide ligands with softer species such as sulfide-, selenide-, or telluride-based ligands results in a red shift. For further reading on these effects, see references [53-61].

Two other possibilities for the PL blue shift have been proposed in prior studies on PB:Si NCs synthesized using thermal precipitation from phosphoborosilicate glass. Such PB:Si NCs exhibit a similar blue-shift in the emission energy after particles are HF-etched from the SiO_2 matrix and suspended in solution.[27, 62] This blue shift has been attributed to both increased quantum confinement (due to HF etching) and fewer P-B pairs (again, resulting from etching), not to any ligand effects.[27, 62] However, we do not believe these mechanisms to be operative for nonthermal plasma-synthesized PB:Si NCs, since dopants would have to be removed from the NC core or, alternatively, the local bonding environment would have to be changed in such a way to render substitutional dopants "inactive" (i.e., trivalent arrangements). Instead, we find that the number of substitutional boron sites in the NC core is unchanged based on our observation that surface functionalization does not modify the (111) diffraction peak position or width (see XRD data in Figure S13). This is to be expected as there is insufficient driving force at ambient temperature to expel NC dopant atoms from the core for covalent semiconductors such as silicon. This high metastability of doped covalent semiconductor NCs such as silicon is a key difference from more ionic semiconductor NCs, such as metal chalcogenides, where impurities are more easily expelled.[13, 14]

Next, we propose that a 3rd mechanism operates to induce a blue shift in L→PB:Si–X NCs relative to solely X-type PB:Si–H and PB:Si–CH_2R NCs. In the modeling work by Delerue,[22] D–A states within PB:Si NCs are still relatively delocalized (characterized by the participation ratio, or degree of coupling between D–A states and Si NC band states), particularly for acceptor states. This is consistent with the experiments here, since otherwise we would not observe a size-dependent shift in the D–A transition energy or effects from ligands on core-residing D–A states without some degree of state coupling. This coupling allows for orbital overlap and the formation of P-B pairs between surface boron and core-residing phosphorus atoms. Invoking molecular orbital (MO) theory,[30] the functional group that coordinates with surface boron sites in P-B pairs will greatly affect the specific energy of the acceptor and donor states (Fig. 5). If this MO picture is valid, the extent of the PL energy shift should be proportional to the electron donating ability of the bonding atom. Experimentally, we find the alcohol (HOR) to induce the greatest shift in the acceptor level, followed by the alkylamine (H_2NR) and then the alkylthiol (HSR), perfectly in line with the electron donating ability of each functional group. As the energy of the acceptor level moves closer to the valence band, the donor level moves higher to compensate. These combined effects cause the D–A transition to be at higher energy than without the L-type interaction, exactly what we observe experimentally for small <4 nm diameter L→PB:Si–X NCs (see Fig. S7b). Similar effects have been observed for II–VI NCs where exchange of electron-donating L-type oleylamine ligands with electron-withdrawing, Lewis acidic Z-type $M(oleate)_2$ (M = Zn, Cd) relaxes quantum confinement, leading to an emission red shift.[63]

We note that at smaller D_{NC} <4 nm, we find the D–A energy levels within alkoxide terminated NCs become degenerate with the bands as evidenced by both the emission energy and the NC lifetimes. As D_{NC} increases, the effect of both X-type and L-type surface coordination becomes weaker due to the shrinking surface-to-volume ratio of the NC; thus, the core-residing P-B pairs are less affected by the surface chemistry/dielectric. This is evidenced by the convergence of the emission energies of X-type and L-type L→PB:Si–X NCs at D_{NC} = 4.8 nm (see Fig. 2b).

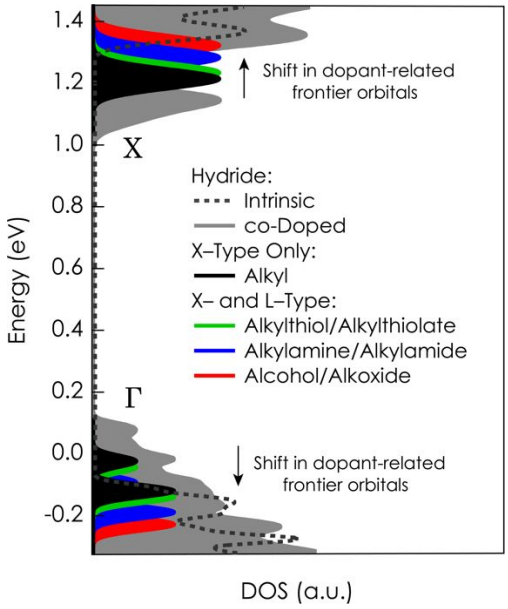

Fig. 5 Density of states (DOS) is shown for both intrinsic (dashed gray line) and co-doped (solid gray) hydrogen-terminated Si NCs as calculated by Delerue.[22] The frontier orbitals associated with both the HOMO and LUMO levels shift upon functionalization with L- and/or X-type ligands.

Conclusions

This work shows that the D–A transitions in PB:Si NCs respond strongly to the surface chemistry. Effects from covalent X-type surface bonding interactions in alkyl PB:Si–CH_2R NCs are found to increase the D–A recombination energy by ~200 meV relative to the as-prepared hydride-terminated NCs PB:Si–H resulting from changes in the potential of dopant-related states. A secondary and equally strong perturbation of the D–A energy levels occurs through L-type Lewis base coordination of surface boron atoms by HOR, H_2NR, and HSR for L→PB:Si–X NCs (X = OR, NHR, SR). This L-type effect can be described by a molecular orbital model, with stronger donor groups leading to a higher energy donor level (closer to the conduction band) and a lower energy acceptor level (closer to the valence band). For both X-type and L-type ligands, an increase in the dielectric environment around the PB:Si

NCs results in less Coulomb screening and, therefore, donor and acceptor states that are closer to the conduction and valence bands, respectively, compared with as-grown PB:Si–H NCs.

These results map out the strong effects of ligands on the D–A levels in PB:Si NCs, all of which result in higher emission energies. For NIR applications, modulating the energetics in the opposite direction (lower energy transitions) is desired. The work presented here details the challenges that must be tackled to achieve lower energy emission. Donors and acceptors with states further from the bands than P and B should be developed. Surface structures with a highly mismatched dielectric to the underlying PB:Si NC core are crucial to ensuring poor Coulomb screening and localization of the states. Similarly, ligands that interact to stabilize the surface but provide weaker Lewis acid-base interactions, thereby weakly perturbing the donor and acceptor levels, should be targeted in future research. Finally, all of these challenges must be overcome while simultaneously achieving high PLQY values that are far from optimized in Si NCs. Still, the future is bright for co-doped PB:Si NCs, which continue to demonstrate fascinating fundamental photophysics while also holding tantalizing promise for future applications.

Conflicts of interest

There are no conflicts to declare.

Acknowledgements

We would like to thank Fernando Urias-Cordero for his help in nanocrystal growth as well as Lance Wheeler for helpful discussion. This work was authored by the National Renewable Energy Laboratory, operated by Alliance for Sustainable Energy, LLC, for the U.S. Department of Energy (DOE) under Contract No. DE-AC36-08GO28308. Funding provided by U.S. Department of Energy Office of Science Chemical Sciences, Geosciences, and Biosciences Solar Photochemistry Program. The views expressed in the article do not necessarily represent the views of the DOE or the U.S. Government. The U.S. Government retains and the publisher, by accepting the article for publication, acknowledges that the U.S. Government retains a nonexclusive, paid-up, irrevocable, worldwide license to publish or reproduce the published form of this work, or allow others to do so, for U.S. Government purposes.

Experimental

General Methods.

All solvents were purchased from Sigma-Aldrich or Fischer, ACS grade or better unless otherwise noted. Toluene and 1-dodecene were distilled from sodium under nitrogen. 1-Dodecylamine, 1-dodecanol, and 1-dodecanethiol were dried under vacuum at 100 °C for 24 hours. All experiments with PB:Si NCs were conducted in an argon-atmosphere glove box, with the exception of powder X-ray diffraction (performed in air; total Si NC air exposure time ≤1 h).

Nanoparticle Growth.

All PB:Si–H NCs in this study were grown via non-thermal plasma synthesis method using a capacitively-coupled 13.56 MHz RF plasma. Using an optimized ratio of process gases $SiH_4/PH_3/B_2H_6$ and carrier gases (Ar, H_2), the NC size was controlled by varying the pressure within the reactor tube. Table S1 summarizes the synthetic methods for all PB:Si NCs reported. Hydrogen-terminated PB:Si NCs (PB:Si–H) were collected downstream from the plasma on a 400-mesh stainless steel filter and transferred via load-lock to an inert-atmosphere argon-filled glovebox for collection and subsequent functionalization/characterization.

CAUTION!! Singly doped and co-doped Si NCs evolve toxic gas (PH_3 and/or B_2H_6) upon air exposure. Rigorous air-free handling is required. Allow samples to air oxidize for at least 1 h in exhaust ventilation before removing into lab ambient.

Surface Functionalization.

As-prepared, Hydride-terminated PB:Si–H NCs were functionalized via hydrosilylation. Approximately 1 mL of each ligand (in this study either 1-dodecene, 1-dodecanethiol, 1-dodecanol, or 1-dodecylamine) was added to 5 mg of PB:Si–H NC powder with the addition ~2 mg 1,1'-azobis(cyclohexanecarbonitrile) (ABCN) radical initiator. The solution was heated at 140–150 °C for ~4 h to ensure saturated ligation. After cooling to ambient temperature, a few mL of dry toluene was added to dilute the sample, and the solution was filtered through a 0.45 μm PTFE filter.

Fourier-Transform Infrared (FTIR) Spectroscopy.

FTIR absorbance measurements were conducted on a Bruker Alpha FTIR spectrometer using a diffuse reflectance infrared Fourier transform spectrometer (DRIFTS) attachment with a resolution of 4 cm^{-1}. Reflective gold-coated polished Si wafers were used for background measurements, and PB:Si–H NCs were deposited by mechanically pressing powder directly onto the same substrates. Spectra were baseline-corrected using the concave rubberband correction method (2 iterations).

Photoluminescence (PL), and Time-Resolved Photoluminescence (TRPL) Spectroscopy.

FTIR absorbance measurements were conducted on a Bruker Alpha FTIR spectrometer using a diffuse reflectance infrared Fourier transform spectrometer (DRIFTS) attachment with a resolution of 4 cm^{-1}. Reflective gold-coated polished Si wafers were used for background measurements, and PB:Si–H NCs were deposited by mechanically pressing powder directly onto the same substrates. Spectra were baseline-corrected using the concave rubberband correction method (2 iterations).

TRPL spectra were collected using a home-built setup in which a Nd:YAG laser was used for photoexcitation and subsequently tuned to the desired wavelength (450 nm) using an optical parametric oscillator (OPO) (Spectra Physics Quanta Ray and GWU Premi Scan). PL spectra were collected in an off-axis, front-face geometry using a Si avalanche photodiode (APD, Thorlabs APD430A). A combination of 650 and 700 longpass filters was used to block the excitation light and the signal from the APD was digitized using a fast oscilloscope (Tektronix DPO7254).

Absolute PL quantum yield (PLQY) measurements were conducted on PB:Si NCs in toluene solution using a fiber-coupled integrating sphere (Labsphere 3P-GPS). A 532 nm collimated laser diode (Thorlabs CPS532-C2) was used as excitation source. The sphere was fibre-coupled, using a Thorlabs M35L02 fibre (Ø1000 μm), to a Princeton HRS-300-SS spectrograph including a PYL100F Si CCD.

X-ray Diffraction.

XRD patterns were taken on a Bruker D8 Discover diffractometer using Cu Kα radiation (λ =1.54 Å). PB:Si NCs were dispersed in toluene slurries on Si-based zero diffractions plates. NC sizes were determined from the XRD spectra by use of the Scherrer-broadening of the (111) diffraction peaks. The NC size was calculated using the equation, $D_{NC} = k \cdot \lambda / w \cdot cos\,(c)$, where D_{NC} is the diameter of the NC, k is a shaping factor of 1.1, λ is the x-ray wavelength (1.54 Å), and w and c are the width and center of the Si (111) diffraction peak in radians, respectively.

Raman Spectroscopy.

Raman spectra of all PB:Si NCs are obtained via an InVia Renishaw confocal Raman microscope with a 532-nm laser and 50X objective lens. The samples are sealed in an air-free holder with a 300 μm-thick transparent sapphire optical window. The data are collected at an output laser power of ~900 uW with 2-second integration time and 5 accumulations.

Notes and references

1. J. M. Caruge, J. E. Halpert, V. Wood, V. Bulović and M. G. Bawendi, *Nat. Photon.*, 2008, **2**, 247.
2. D. V. Talapin, J.-S. Lee, M. V. Kovalenko and E. V. Shevchenko, *Chem. Rev.*, 2010, **110**, 389.
3. H. Lu, G. M. Carroll, N. R. Neale and M. C. Beard, *ACS Nano*, 2019, **13**, 939.
4. R. Mazzaro, F. Romano and P. Ceroni, *Phys. Chem. Chem. Phys.*, 2017, **19**, 26507.
5. B. G. Lee, J.-W. Luo, N. R. Neale, M. C. Beard, D. Hiller, M. Zacharias, P. Stradins and A. Zunger, *Nano Letters*, 2016, **16**, 1583.
6. F. Meinardi, S. Ehrenberg, L. Dhamo, F. Carulli, M. Mauri, F. Bruni, R. Simonutti, U. Kortshagen and S. Brovelli, *Nat. Photon.*, 2017, **11**, 177.
7. M. L. Mastronardi, F. Maier-Flaig, D. Faulkner, E. J. Henderson, C. Kübel, U. Lemmer and G. A. Ozin, *Nano Lett.*, 2012, **12**, 337.
8. D. M. Kroupa, B. K. Hughes, E. M. Miller, D. T. Moore, N. C. Anderson, B. D. Chernomordik, A. J. Nozik and M. C. Beard, *J. Am. Chem. Soc.*, 2017, **139**, 10382.
9. H. Lu, G. M. Carroll, X. Chen, D. K. Amarasinghe, N. R. Neale, E. M. Miller, P. C. Sercel, F. A. Rabuffetti, A. L. Efros and M. C. Beard, *J. Am. Chem. Soc.*, 2018, **140**, 13753.
10. H. Zhang, R. Zhang, K. S. Schramke, N. M. Bedford, K. Hunter, U. R. Kortshagen and P. Nordlander, *ACS Photonics*, 2017, **4**, 963.
11. M. Fujii, S. Hayashi and K. Yamamoto, *J. Appl. Phys.*, 1998, **83**, 7953.
12. A. Mimura, M. Fujii, S. Hayashi, D. Kovalev and F. Koch, *Phys. Rev. B*, 2000, **62**, 12625.
13. G. Galli, *Nature*, 2005, **436**, 32-33.
14. S. C. Erwin, L. Zu, M. I. Haftel, A. L. Efros, T. A. Kennedy and D. J. Norris, *Nature*, 2005, **436**, 91.
15. X. D. Pi, R. Gresback, R. W. Liptak, S. A. Campbell and U. Kortshagen, *Appl. Phys. Lett.*, 2008, **92**, 123102.
16. D. J. Rowe, J. S. Jeong, K. A. Mkhoyan and U. R. Kortshagen, *Nano Lett.*, 2013, **13**, 1317.
17. N. J. Kramer, K. S. Schramke and U. R. Kortshagen, *Nano Lett.*, 2015, **15**, 5597.
18. B. T. Diroll, K. S. Schramke, P. Guo, U. R. Kortshagen and R. D. Schaller, *Nano Lett.*, 2017, **17**, 6409.

19. R. Limpens and N. R. Neale, *Nanoscale*, 2018, **10**, 12068.
20. R. Limpens, G. F. Pach, D. W. Mulder and N. R. Neale, *J. Phys. Chem. C*, 2019, **123**, 5782.
21. R. Limpens, G. F. Pach and N. R. Neale, *Chem. Mater.*, 2019, **31**, 4426.
22. C. Delerue, *Phys. Rev. B*, 2018, **98**, 045434.
23. N. X. Chung, R. Limpens, A. Lesage, M. Fujii and T. Gregorkiewicz, *Phys. Status Solidi A*, 2016, **213**, 2863.
24. M. Fujii, K. Toshikiyo, Y. Takase, Y. Yamaguchi and S. Hayashi, *J. Appl. Phys.*, 2003, **94**, 1990.
25. M. Fujii, Y. Yamaguchi, Y. Takase, K. Ninomiya and S. Hayashi, *Appl. Phys. Lett.*, 2004, **85**, 1158.
26. Y. Hori, S. Kano, H. Sugimoto, K. Imakita and M. Fujii, *Nano Lett.*, 2016, **16**, 2615.
27. H. Sugimoto, M. Fujii, K. Imakita, S. Hayashi and K. Akamatsu, *J. Phys. Chem. C*, 2013, **117**, 11850.
28. R. Limpens, M. Fujii, N. R. Neale and T. Gregorkiewicz, *J. Phys. Chem. C*, 2018, **122**, 6397.
29. D. M. Kroupa, M. Vörös, N. P. Brawand, B. W. McNichols, E. M. Miller, J. Gu, A. J. Nozik, A. Sellinger, G. Galli and M. C. Beard, *Nat. Commun.*, 2017, **8**, 15257.
30. N. C. Anderson, M. P. Hendricks, J. J. Choi and J. S. Owen, *J. Am. Chem. Soc.*, 2013, **135**, 18536.
31. J. Owen, *Science*, 2015, **347**, 615.
32. K. A. Littau, P. J. Szajowski, A. J. Muller, A. R. Kortan and L. E. Brus, *J. Phys. Chem.*, 1993, **97**, 1224.
33. M. Dasog, Z. Yang, S. Regli, T. M. Atkins, A. Faramus, M. P. Singh, E. Muthuswamy, S. M. Kauzlarich, R. D. Tilley and J. G. C. Veinot, *ACS Nano*, 2013, **7**, 2676.
34. L. M. Wheeler, N. R. Neale, T. Chen and U. R. Kortshagen, *Nat. Commun.*, 2013, **4**, 2197.
35. H. Li, Z. Wu, T. Zhou, A. Sellinger and M. T. Lusk, *Phys. Chem. Chem. Phys.*, 2014, **16**, 19275.
36. T. Zhou, R. T. Anderson, H. Li, J. Bell, Y. Yang, B. P. Gorman, S. Pylypenko, M. T. Lusk and A. Sellinger, *Nano Lett.*, 2015, **15**, 3657.
37. M. Dasog, K. Bader and J. G. C. Veinot, *Chem. Mater.*, 2015, **27**, 1153.
38. G. M. Carroll, R. Limpens and N. R. Neale, *Nano Lett.*, 2018, **18**, 3118.
39. G. M. Carroll, R. Limpens, G. F. Pach and N. R. Neale, 2019, In Preparation.
40. J.-W. Luo, P. Stradins and A. Zunger, *Energ. Environ. Sci.*, 2011, **4**, 2546.
41. L. D. Negro, S. Hamel, N. Zaitseva, J. H. Yi, A. Williamson, M. Stolfi, J. Michel, G. Galli and L. C. Kimerling, *IEEE J. Sel. Top. Quantum Electron.*, 2006, **12**, 1151.
42. J. M. Buriak, *Chem. Mater.*, 2014, **26**, 763.
43. L. M. Wheeler, N. C. Anderson, P. K. B. Palomaki, J. L. Blackburn, J. C. Johnson and N. R. Neale, *Chem. Mater.*, 2015, **27**, 6869.
44. M. L. H. Green, *J. Organomet. Chem.*, 1995, **500**, 127.
45. J. Ma, S.-H. Wei, N. R. Neale and A. J. Nozik, *Appl. Phys. Lett.*, 2011, **98**, 173103.
46. K. Nomoto, H. Sugimoto, A. Breen, A. V. Ceguerra, T. Kanno, S. P. Ringer, I. P. Wurfl, G. Conibeer and M. Fujii, *J. Phys. Chem. C*, 2016, **120**, 17845.
47. L. M. Wheeler, N. J. Kramer and U. R. Kortshagen, *Nano Lett.*, 2018, **18**, 1888.
48. H. Sugimoto, M. Yamamura, R. Fujii and M. Fujii, *Nano Lett.*, 2018, **18**, 7282.
49. A. Marchioro, P. J. Whitham, K. E. Knowles, T. B. Kilburn, P. J. Reid and D. R. Gamelin, *J. Phys. Chem. C*, 2016, **120**, 27040.
50. D. M. Sagar, J. M. Atkin, P. K. B. Palomaki, N. R. Neale, J. L. Blackburn, J. C. Johnson, A. J. Nozik, M. B. Raschke and M. C. Beard, *Nano Lett.*, 2015, **15**, 1511.
51. L. Mangolini and U. Kortshagen, *Adv. Mater.*, 2007, **19**, 2513.
52. B. Somogyi, E. Bruyer and A. Gali, *J. Chem. Phys.*, 2018, **149**, 154702.
53. R. D. Harris, S. Bettis Homan, M. Kodaimati, C. He, A. B. Nepomnyashchii, N. K. Swenson, S. Lian, R. Calzada and E. A. Weiss, *Chem. Rev.*, 2016, **116**, 12865.
54. M. T. Frederick and E. A. Weiss, *ACS Nano*, 2010, **4**, 3195.
55. M. T. Frederick, V. A. Amin, L. C. Cass and E. A. Weiss, *Nano Lett.*, 2011, **11**, 5455.
56. M. B. Teunis, S. Dolai and R. Sardar, *Langmuir*, 2014, **30**, 7851.
57. C. Giansante, I. Infante, E. Fabiano, R. Grisorio, G. P. Suranna and G. Gigli, *J. Am. Chem. Soc.*, 2015, **137**, 1875.
58. H. Zhang, B. Hu, L. Sun, R. Hovden, F. W. Wise, D. A. Muller and R. D. Robinson, *Nano Lett.*, 2011, **11**, 5356.
59. J. J. Buckley, E. Couderc, M. J. Greaney, J. Munteanu, C. T. Riche, S. E. Bradforth and R. L. Brutchey, *ACS Nano*, 2014, **8**, 2512.
60. B. K. Hughes, D. A. Ruddy, J. L. Blackburn, D. K. Smith, M. R. Bergren, A. J. Nozik, J. C. Johnson and M. C. Beard, *ACS Nano*, 2012, **6**, 5498.
61. K. J. Schnitzenbaumer, T. Labrador and G. Dukovic, *J. Phys. Chem. C*, 2015, **119**, 13314-13324.
62. H. Sugimoto, M. Fujii, K. Imakita, S. Hayashi and K. Akamatsu, *J. Phys. Chem. C*, 2013, **117**, 6807.
63. Y. Zhou, F. Wang and W. E. Buhro, *J. Am. Chem. Soc.*, 2015, **137**, 15198.

